[1]H. D. Hagstrum, Phys. Rev. 150, 495 (1966).
[2]H. D. Hagstrum and G. E. Becker, Phys. Rev. 159, 572 (1967).
[3]H. D. Hagstrum, J. Res. Natl. Bur. Std. 74A, 433 (1970).
[4]H. D. Hagstrum and G. E. Becker, J. Chem. Phys. 54, 1015 (1971).
[5]J. J. Lander, Phys. Rev. 91, 1382 (1953).
[6]H. D. Hagstrum, Y. Takeishi, and D. D. Pretzer, Phys. Rev. 139, A526 (1965).
[7]V. F. Turchin, V. P. Kozlov, and M. S. Malkevich, Usp. Fiz. Nauk. 102, 345 (1970)[Sov. Phys. Usp. 13, 681 (1971)].
[8]R. B. Blackman (private communication).
[9]W. M. Gentleman (private communication). See W. M. Gentleman and G. Sande, in *Proceedings of the Fall Joint Computer Conference, November*, 1966 (Spartan Books, Washington, D. C., 1966), AFIPS Conf. Proc. 29, 563 (1966).
[10]G. F. Amelio and E. J. Scheibner, Surface Sci. 11, 242 (1968).
[11]G. F. Amelio, Surface Sci. 22, 301 (1970).

PHYSICAL REVIEW B VOLUME 4, NUMBER 12 15 DECEMBER 1971

Azbel'-Kaner Cyclotron Resonance in Mercury†

R. G. Poulsen* and W. R. Datars
Department of Physics, McMaster University, Hamilton, Ontario, Canada
(Received 1 July 1971)

Azbel'-Kaner cyclotron-resonance experiments have been carried out with two very flat mercury crystals at a microwave frequency of 34.28 GHz and a temperature of 1.2 °K. Cyclotron effective masses of ten orbits were measured with an error of less than 2%. Five of the orbits (labeled μ_γ, γ_2, κ, μ_2, and ϵ_1) were observed for the first time by Azbel'-Kaner cyclotron resonance. The cyclotron masses of α orbits in the electron lenses were represented by an interpolation scheme which gives the mass for any field direction. This interpolation scheme showed that the second-zone electron lens is tipped 3° out of a (100) plane of the reciprocal lattice toward the [111] direction and that there is a 9% anisotropy of the mass in the (100) plane. A similar interpolation scheme describing the frequencies of de Haas–van Alphen (dHvA) oscillations, which correspond to the β arms of the first-zone hole surface, is also presented. The oscillations were caused by two effects which could not be separated: quantum oscillations of the microwave surface impedance and dHvA torque. Methods for accurately determining the crystal orientation within the experimental apparatus, using the symmetry of the electron-lens masses and of signal peaks arising from open-orbit induced-torque effects, are presented. Cyclotron resonance with the magnetic field inclined to the sample surface is discussed. Several effects indicate anomalous penetration of the electromagnetic field into the metal.

I. INTRODUCTION

The cyclotron effective mass in a metal is proportional to the derivative with respect to energy of the area of a cyclotron orbit and is greater than that determined from the band structure because of mass enhancements arising from electron-electron and electron-phonon interactions.[1] However, contributions of electron-electron interactions to the cyclotron mass are often partially folded into band-structure calculations,[2] and are small and independent of energy and temperature.[3] Thus, in addition to providing information concerning Fermi-surface topology, determinations of the cyclotron mass also yield information about electron-phonon mass enhancement. This is particularly important for mercury in which there is a large electron-phonon interaction. The cyclotron mass, the electron-phonon mass enhancement factor $1+\lambda$, and their variations with temperature and energy are conveniently measured by Azbel'-Kaner cyclotron resonance.

Azbel'-Kaner cyclotron resonance (AKCR) is observed by shining microwave radiation on the surface of a flat metal sample in the presence of an applied magnetic field aligned parallel to the sample surface.[4] Electrons spiraling along the magnetic field direction return an average of $\omega_c\tau/2\pi$ times to the skin depth region at the sample surface. $\omega_c = eH/m_c c$ is the cyclotron frequency, H is the magnetic field, and m_c and τ are the cyclotron mass and relaxation time, respectively. Resonance occurs when electrons and the rf microwave field are in phase for successive cyclotron revolutions. This occurs at fields $H_N = c\omega m_c/Ne$ (N is an integer) for which the microwave frequency ω is equal to, or an integral multiple of, ω_c. The reciprocal fields $1/H_N$ are periodic.

Azbel' and Kaner have shown that, with appropriate orientation of the x and y axes in the sample surface, the surface impedance $Z(H)$ is

$$Z_{xx,yy}(H) = Z_{xx,yy}(0)\left[1 - \exp\left(-2\pi i\omega/\omega_c - 2\pi/\omega_c\tau\right)\right]^{1/3} \quad (1)$$

for electrons of common mass, where $Z(0)_{xx,yy}$ is

the zero-field anomalous surface impedance for microwave polarizations along x or y and is complex, containing the factor $e^{+i\pi/3}$. Chambers[5] has shown that there may be contributions to Eq. (1) from nonresonant electrons when the Fermi surface is not a simple closed convex surface. The resonances are best defined by peaks of the field derivative dR/dH of the surface resistance at fields H_N.[6] Then the mass is determined from

$$m_c = \frac{e}{c\omega\Delta(1/H)} , \qquad (2)$$

where $\Delta(1/H)$ is the slope of a straight line which is fitted, in a least-squares sense, to a plot of $1/H_N$ vs N. Equation (2) is accurate in the limit that the relaxation time τ tends to infinity; as τ decreases the resonance fields H_N shift to higher fields. Then, because the shifts for low N are proportionately larger than those for large N, the plot of $1/H_N$ vs N is no longer linear and masses predicted from Eq. (2) are high. The error in the determined mass decreases as the number of resonance peaks included in the least-squares fit is increased. Changes of the peak positions and the resulting mass error due to finite $\omega\tau$, computed using Eqs. (1) and (2) for electrons of common mass, are shown in Fig. 1. The values of $\omega\tau$ in Fig. 1 are approximately those found for the α orbit in mercury at temperatures of 1.15 and 2.1 °K.[7] The error in m_c, computed for a series of up to N resonance peaks, is seen to be less than the shift of the Nth resonance peak and is always less than 1.5% for $\omega\tau = 20$.

The line shape of AKCR varies spectacularly when the field $\vec{H}$ is tipped an angle α out of the sample surface.[8] In mercury for $\alpha \lesssim 1°$, the resonances are found to broaden, shift to lower or higher fields, or even split in two as α increases. Aside from being interesting in their own right, such tipping effects, by their symmetry for positive and negative tip angles, provide sensitive indicators with which to align $\vec{H}$ parallel to the sample surface and to set limits on the surface flatness. Such accurate alignment (and samples flat to the order of minutes of arc) is necessary in order to measure accurate cyclotron masses because generally the resonance peaks for low N are more sensitive to tipping effects than those for large N.

The purpose of this paper is to present accurate measurements of the cyclotron masses of AKCR for two very flat mercury crystals. The measured masses are assigned to ten orbits, five of which had not previously been observed by AKCR. Masses of orbits on the electron lenses are represented by an interpolation scheme. The mass measurements allow estimates of the magnitude of the electron-phonon mass enhancement in mercury. In other publications,[7] we have reported studies of the temperature dependence of the electron-phonon contributions to the cyclotron mass and the relaxation time. The present work provides some background information to supplement the discussion of this other work.

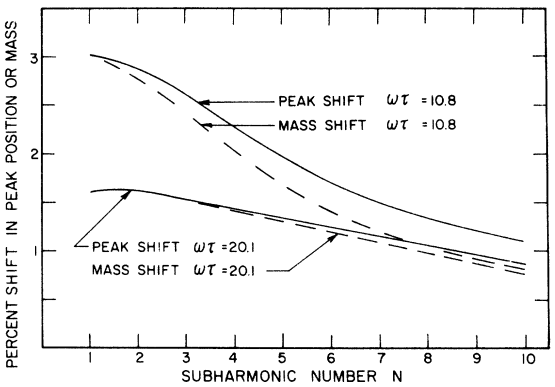

FIG. 1. Solid curves show the changes in the resonance peak positions for $\omega\tau = 10.8$ and 20.1 from those for infinite $\omega\tau$. The dashed curves show the error in mass resulting by assuming $\omega\tau = \infty$ and using Eq. (2) as a function of the number of subharmonics used in the calculation.

Cyclotron resonance in mercury was first observed using the slightly curved free surface of mercury crystals.[9] Large cyclotron-resonance signals were observed but, because of the use of curved sample surfaces, some resonances were not found and the resonance lines were shifted and distorted giving rise to the possibility of errors in the reported masses as a result of field-tipping effects. The present new measurements were made possible by growing mercury crystals on optically flat surfaces.

Recently, other experimental methods have also been used to investigate the Fermi surface of mercury. Magnetoresistance experiments by Datars and Dixon[10] and Dishman and Rayne[11] provided information about the open orbits in mercury. Extremal calipers of the surface have been determined from magnetoacoustic data by Bogle *et al.*[12] The de Haas–van Alphen (dHvA) effect experiments by Brandt and Rayne[13] and Poulsen, Moss, and Datars[14] provided extremal cross-sectional areas of the surface. These experimental results are in general accord with the Fermi-surface topology predicted by Keeton and Loucks[15] from a relativistic augmented-plane-wave (RAPW) calculation. The Fermi surface described by pseudopotential calculations[11,13,16] is topologically equivalent to the Keeton-Loucks model. These calculations suggest required modifications to the nearly-free-electron model to make it useful for considering possible extremal orbits in mercury. Some orbits on this model have been described in previous work.[9,12,14] Again, we make use of the modified nearly-free-electron model for the analysis of the cyclotron-

resonance results and the description of several new extremal orbits in mercury.

II. EXPERIMENTAL METHOD

The cyclotron-resonance data were taken with a Varian model No. V-4503 EPR microwave spectrometer operated at 34.28 GHz. Flat mercury single crystals formed the end wall of a cylindrical TE_{113} resonant cavity which was side coupled to the broad face of an 8-mm rectangular waveguide suspended vertically between the pole faces of a 0–20-kOe electromagnet. A tunable shorting plunger terminated the waveguide below the cavity and allowed the cavity coupling, and hence the spectrometer sensitivity, to be adjusted during an experiment. The microwave currents in the sample surface were polarized vertically in the sample surface by a copper stirrup positioned horizontally across the iris hole of the cavity. This polarization was shown to be greater than 90% by measuring the electron-spin resonance signals from a uniform dispersion of diphenylpicrylhydrazyl (DPPH) on the surface of a copper test sample first with $\vec{H} \perp \vec{H}_{rf}$, and then with $\vec{H} \parallel \vec{H}_{rf}$, where $\vec{H}_{rf}$ was the microwave $\vec{H}$ field. The cavity was split in the center so that the half containing the sample could be rotated about the axis of the cavity by a gear drive mechanism. By rotating the magnet and the cavity, the tip angle between the applied field $\vec{H}$ and any direction in the sample surface was varied and measurements could be made in any crystallographic direction. Large tip angles were measured with an accuracy of $\pm 0.2°$ using a precision potentiometer attached to the magnet base. An optical lever arrangement, using the image of a fine crosshair projected via a mirror mounted on the magnet (and two fixed mirrors to fold the optical path) onto a nearby wall, was used for small tip angle measurements with a resolution of $\pm 0.005°$. For cyclotron-resonance studies, the field was aligned to within $\pm 0.02°$ of the sample surface by setting it at the position about which the small-angle field-tipping effects were symmetrical.

Measurements were carried out with the cavity and sample immersed directly in the helium bath at temperatures as low as 1.1 °K. Changes in spectrometer sensitivity caused by helium-level changes in the waveguide were eliminated by placing a cellulose tape seal over the end of a waveguide flange just above the cavity and evacuating the waveguide above it.

The field derivative dR/dH of the surface resistance R was recorded as a function of magnetic field strength and magnetic rotation angle on a strip chart recorder. The field was measured with 0.2% accuracy by a rotating-coil gaussmeter calibrated with an nuclear magnetic resonance (NMR) gaussmeter.

The samples were flat single-crystal discs approximately 16 mm in diameter and 5 mm thick and were grown from 99.9999% pure mercury. The crystals were grown in a chlorotrifluoethylene (Kel-F) mould between glass slides by freezing mercury while in a controlled temperature gradient. The glass slides were covered with a thin ($\lesssim 1\ \mu$) coating of paraffin wax to reduce the possibility of surface damage arising from differential thermal contraction between the glass and the mercury and to facilitate easy removal after crystal growth. The crystals were held firmly against the end of the cylindrical cavity using a stiff phosphor bronze spring with a backing plate placed between the crystal and spring to minimize damage to the crystal. The specimens were mounted on the cavity in liquid nitrogen in a specially constructed dry room to prevent frost accumulation on the sample surface or between the sample and cavity.

The orientations of the samples were determined to better than 0.5° within the experimental apparatus by using sharp peaks, such as those shown in Fig. 2, which were observed when the magnet was rotated at constant field and angular velocity. These peaks were found to occur whenever the magnetic field passed through planes normal to open-orbit directions. Thus, the crystal orientation could be accurately determined from a least-squares fit of a three-dimensional stereogram of the observed peak positions to the known open-orbit pattern[10,11] for mercury. The peaks themselves were attributed to changes in the cavity Q resulting from torque on the sample arising from the interaction of the applied field and eddy currents induced in the sample by the magnetic field modulation. The peaks occurred because the induced current is small except for field directions perpendicular to an open-orbit direction where the torque is determined by the open-orbit conductivity.[17]

The orientations of two samples were 12° and 20° from the $(1\bar{1}0)$ planes as shown in Fig. 3. In Fig. 3, the normals $N(\theta, \phi)$ to the sample surfaces have co-

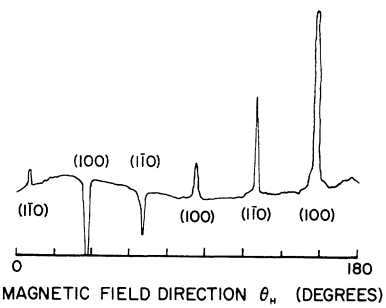

FIG. 2. Peaks in the field derivative of the surface resistance arising from open-orbit induced-torque effects. Assignment to open orbits is shown.

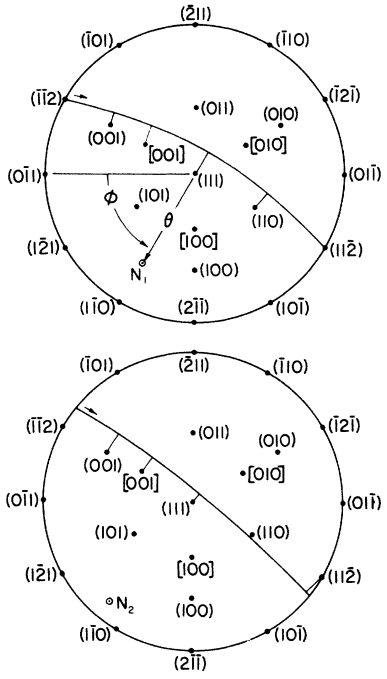

FIG. 3. Stereographic projections on the (111) plane of the orientations of the sample surfaces of samples No. 1 and No. 2. N_1 and N_2 are the normal directions to the sample surfaces.

ordinates (θ, ϕ) of (69.7°, 59.9°) for sample No. 1, and (82.1°, 51.5°) for sample No. 2. The great circles represent the sample surfaces and the thin lines between (lmn) directions, and the sample surfaces indicate the positions of the projections $P(lmn)$ of several (lmn) directions onto the sample surface. In this paper, field directions in the sample surface are specified by angles θ_s measured relative to the projection of the $(\bar{1}\bar{1}2)$ direction on the sample surface in the sense shown by the arrows in Fig. 3. We adopt the notation[15] that (lmn) represents a direction in reciprocal space, or a plane in real space perpendicular to the (lmn) direction. Real space directions are represented by $[lmn]$. Sets of equivalent directions are represented by $\{lmn\}$ in reciprocal space and by $\langle lmn\rangle$ in real space.

A typical AKCR trace for mercury is shown in Fig. 4 for sample No. 2 at 1.1 °K with $\vec{H}$ in the sample surface at $\theta_s = 90.0°$. Six distinct resonances are involved. The dominant resonance in this trace was the resonance used for the study of the temperature dependence of cyclotron mass and relaxation time.[7] This resonance corresponded to the nearly ellipsoidal second-zone electron lens normal to the (001) direction. It was dominant because a wide band of electrons of common mass on the nearly ellipsoidal lens contributed in phase to the resonance and because the flat portion of the real-space electron trajectories was parallel to the sample surface. Such electrons are said to have a very favorable geometrical factor and interact strongly with the applied rf microwave field. The trace in Fig. 4 also shows a signal from DPPH at 12.22 kOe and a sharp peak, which saturated the spectrometer, from the superconducting transition at 0.35 kOe. Similar traces were taken at intervals in θ_s of 2.5°. There were frequent checks of the small-angle tipping effects to ensure accurate alignment of the field to the sample surface in order to minimize errors arising from field-tipping effects in mass values determined from Eq. (2). Such errors were less than 1% because samples No. 1 and No. 2 were flat to better than 12 and 3 min of arc, respectively, and the $N=1$ resonance peaks from the various orbits shifted less than 10%/deg of field tip from the sample surface. The electron-phonon limited value of $\omega\tau$ of approximately 20 also caused errors. Thus, the masses are expected to be accurate to ± 2%.

The field was aligned to within ± 0.02° of the sample surface by locating the tip angle about which the field-tipping effects were symmetrical. Crystal flatness was determined qualitatively by measuring the angular range of tip on either side of the symmetry point for which the $N=1$ peak of the most tip sensitive resonance series was not noticeably broadened or shifted in field. For $\vec{J}_{rf} \perp \vec{H}$, the electron-lens resonance series responsible for the dominant resonance in Fig. 4 was most useful for such estimates over wide ranges of θ_s. Because the flatness was specified by tip angles at which tip effects were first apparent, the crystals were probably somewhat flatter than estimated.

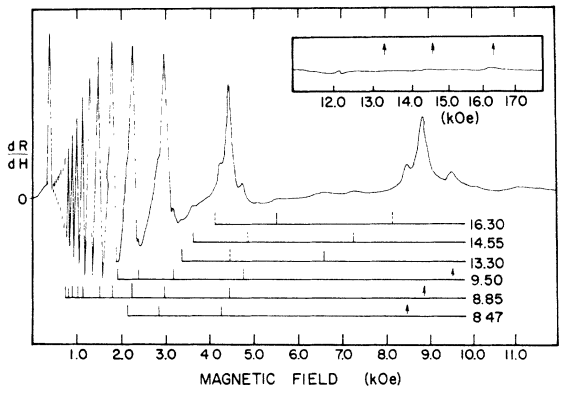

FIG. 4. Typical AKCR trace for mercury. The region from 12 to 17 kOe is inset at the top right-hand corner. The trace shows resonance series with fundamental resonances at fields of 8.47, 8.84, 9.50, 13.30, 14.50, and 16.30 kOe. Subharmonic sets for each of these series are indicated by sets of vertical lines below the trace. In each set the fundamental resonance is indicated by an arrow, and peaks obscured by larger ones are represented by dashed lines.

III. CYCLOTRON MASS MEASUREMENTS

A. Cyclotron Effective Masses and Orbit Assignments

Effective-mass curves for samples No. 1 and No. 2 are shown in Figs. 5 and 6. Points denoted by crosses were obtained from $N=1$ resonance peaks only, and were included only because they appeared to be extensions of well-defined mass curves. A number of low-amplitude peaks for which no subharmonic series could be found were disregarded because of the possibility that they might not be due to AKCR. Plots of $1/H_N$ vs N were found to intersect the N axis at $|\Delta N| \lesssim 0.03$ for both samples. ΔN was not systematically negative as expected for finite $\omega\tau$. These shifts were therefore attributed to errors in determining magnetic field values of dR/dH peaks.

For convenience in subsequent discussion, the notation X^y_z will be used to identify the mass curve X and to convey the information that this branch corresponds to sample No. y and is attributed to the cyclotron orbit z. Descriptions of the orbits have been given by Poulsen *et al.*[14] and Bogle *et al.*[12]

Mass curves S^1_α and D^2_α corresponded to the dominant signals, for their respective samples, with over ten resonance peaks visible at every field direction. Signals corresponding to T^1_α, V^1_α, F^2_α, and G^2_α were considerably weaker, so that typically only four or five resonances were observed. These six mass curves are attributed to α orbits on the electron lenses because they could be observed through 180° of field rotation, indicating closed surfaces, and because each was at a maximum near the angle of closest approach of $\vec{H}$ to a {100} axis. S^1_α and D^2_α, and indeed all of the α-orbit mass curves, reach their maxima at field directions several degrees from the projection of the (100) direction in reciprocal space on the sample surface. These shifts indicate the electron-lens mass maxima are tipped approximately 3° from the (100) direction toward the (111) direction; this will be confirmed later using an empirical interpolation scheme fitted to the α-orbit data for both samples.

The mass curves U^1_γ and H^2_γ were both characterized by four or five observable resonance peaks. These mass curves are attributed to the γ orbits approximately normal to the (110) direction of reciprocal space in Fig. 3; the positions of the minima

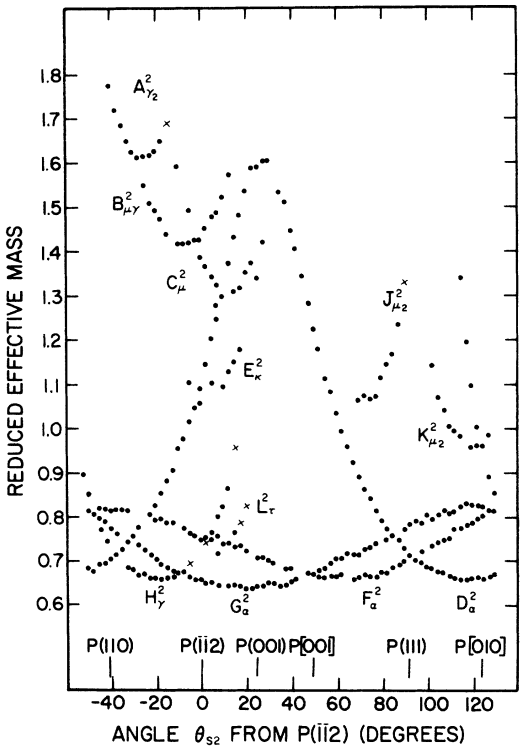

FIG. 6. Cyclotron effective masses measured with sample No. 2. $P(110)$, $P(\bar{1}\bar{1}2)$, $P(001)$, $P(111)$, and $P(010)$ show the projections of the (110), $(\bar{1}\bar{1}2)$, (001), (111), and (010) directions in reciprocal space on the sample surface, respectively, and $P[001]$ shows the projection of the [001] direction in real space.

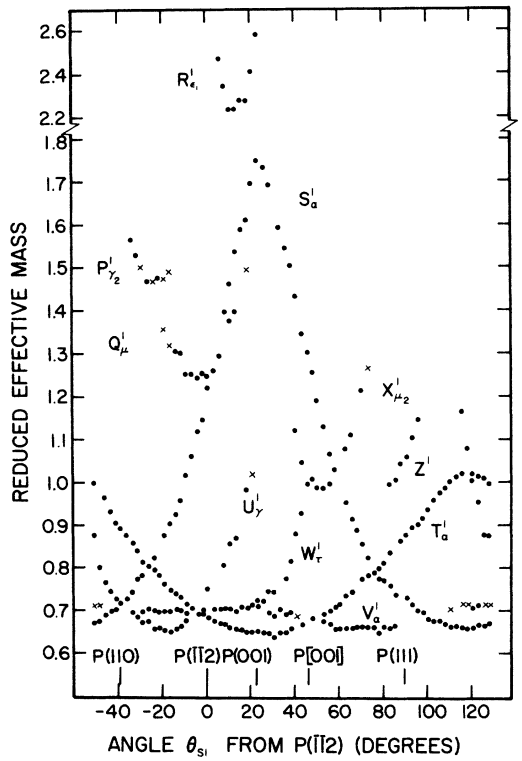

FIG. 5. Cyclotron effective masses measured with sample No. 1. $P(110)$, $P(\bar{1}\bar{1}2)$, $P(001)$, and $P(111)$ show the projections of the (110), $(\bar{1}\bar{1}2)$, (001), and (111) directions in reciprocal space on the sample surface, respectively and $P[001]$ shows the projection of the [001] direction in real space.

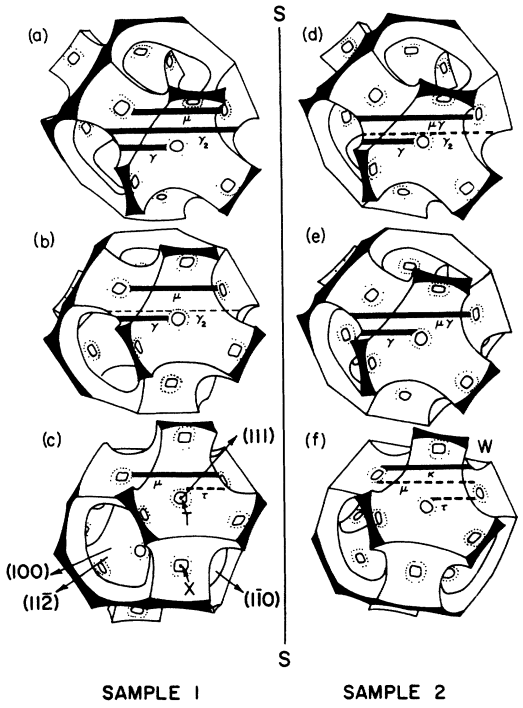

FIG. 7. Orbits on the hole surface of the nearly-free-electron model for several orientations corresponding to samples No. 1 and No. 2. For each orientation, the sample surface, represented by the line S-S, is perpendicular to the plane of the drawing, and the applied field $\vec{H}$ is in the sample surface and parallel to S-S. The Fermi-surface orbits are in planes perpendicular to $\vec{H}$. The angles θ_s, which specify the orientations of $\vec{H}$ relative to the projection of the ($1\bar{1}2$) direction on the sample surface are approximately $-22°$, $0°$, and $+15°$ in (a)–(c), respectively (for sample No. 1), and $-25°$, $-15°$, and $+10°$ in (d)–(f), respectively (for sample No. 2).

for these curves and their relatively large ranges agree qualitatively with predictions[14] for the γ orbit. These mass curves show that the minimum γ-orbit mass is $18° \pm 2°$ from the ($11\bar{2}$) direction in reciprocal space toward the (110) direction in the ($1\bar{1}0$) plane, with a value $m^*/m_0 = 0.65$. At the projection of the ($11\bar{2}$) direction on the sample surface, the m^*/m_0 for both U^1_γ and H^2_γ is approximately 0.73; this confirms the assignment to the γ orbit by Dixon and Datars[9] of the mass curves D, E, and F of their Fig. 6.

Mass curves $P^1_{\gamma_2}$, Q^1_μ, $R^1_{\epsilon_1}$, $A^2_{\gamma_2}$, $B^2_{\mu\gamma}$, and C^2_μ corresponded to weaker signals for which typically only five resonance peaks were observed. Only two or three resonance peaks corresponding to E^2_κ were observed. Assignments of orbits to these mass curves were made with the aid of Fig. 7, which shows several views of the nearly-free-electron model[9] for orientations corresponding to samples No. 1 and No. 2. Figure 7(c) is marked in accord with Fig. 2 of Poulsen *et al.*[14] in which the X- and T-face openings of the hole surface and the crystallographic axes are labeled. The solid lines around X and T represent the sizes of the breakthrough regions at X and T predicted by Keeton and Loucks[15] and the dotted lines represent those predicted by the Mag V model of Dishman and Rayne.[11]

Figures 7(d)–7(f) are for orientations near the minima of mass curves $A^2_{\gamma_2}$, $B^2_{\mu\gamma}$, and C^2_μ, respectively. $A^2_{\gamma_2}$ is assigned to a γ_2 orbit because this orbit may exist for Fig. 7(d), but probably does not exist for Fig. 7(e), and cannot exist for Fig. 7(f). Similarly, mass curve $B^2_{\mu\gamma}$ is assigned to a $\mu\gamma$ orbit because this orbit is probably possible for Fig. 7(e), and should exist for Fig. 7(d). Mass curve C^2_μ is assigned to a μ orbit, which can exist for Figs. 7(e) and 7(f) if the X-face openings are just slightly larger than the size predicted by Dishman and Rayne.[11] Mass curve E^2_κ is assigned to a κ orbit, which cannot exist for Figs. 7(d) and 7(e), but should exist for a small angular range near the projection of the ($11\bar{2}$) direction on the sample surface in Figs. 6 and 7(f). This orbit is expected to cut off, as does mass curve E^2_κ, because as the field is rotated toward the projection of the (110) direction on the sample surface the orbit can no longer pass between the two β arms near the point W in Fig. 7(f). It is fortuitous that the orientation of sample No. 2 allowed the observation of all these orbits for fields in the sample surface.

Figures 7(a)–7(c) are for orientations near the minima of mass curves $P^1_{\gamma_2}$, Q^1_μ, and $R^1_{\epsilon_1}$, respectively. Mass curve $P^1_{\gamma_2}$ is assigned to a γ orbit since this orbit can exist for Fig. 7(a), is less likely to exist for Fig. 7(b), and cannot exist for Fig. 7(c). Similarly, mass curve Q^1_μ is assigned to a μ orbit, which may just exist for Fig. 7(a), reaches its minimum for Fig. 7(b), and can still exist for Fig. 7(c). Mass curve $R^1_{\epsilon_1}$ is tentatively assigned to the ϵ_1 orbit[12] for $\vec{H}$ near the (001) direction in reciprocal space. This orbit circumvents the first-zone electron neck through the L face for a limited angular range of $\vec{H}$ near the (001) direction; it is surprising that this orbit could be observed when $\vec{H}$ passed only within $8.2°$ of the (001) direction, and that it could be observed over a range of $15°$. However, there appears to be no other explanation for this mass curve.

The assignments of γ_2, $\mu\gamma$, μ, and κ orbits near the projection of the ($1\bar{1}2$) direction of reciprocal space on the sample surface are strengthened by the observation that, as the orientation changes from that of sample No. 2 to that of sample No. 1, the minimum masses for the γ_2 and μ orbits are expected to decrease and signals for the $\mu\gamma$ and κ orbits are expected to disappear, as observed. Also, for the nearly-free-electron model, the mass corresponding to γ_2 is expected to be more than double that of γ for $\vec{H}$ near the ($1\bar{1}2$) direction as observed

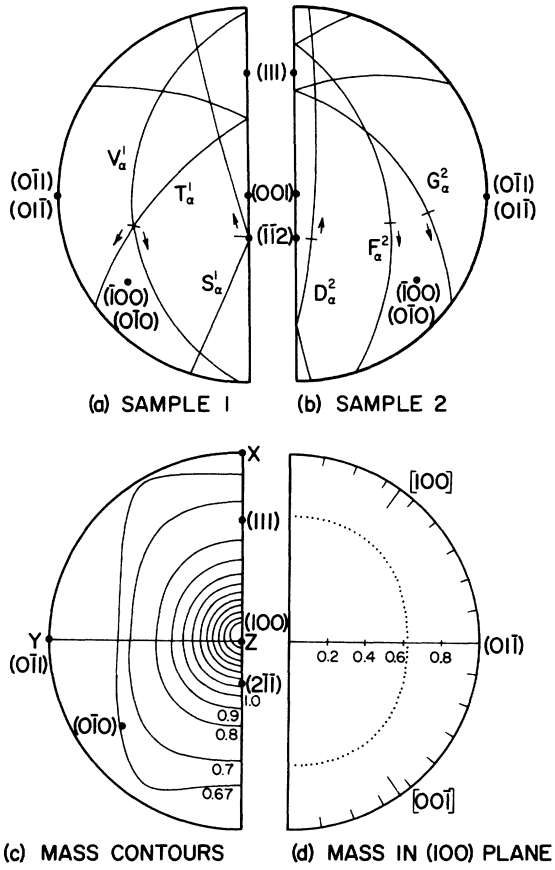

FIG. 8. (a) Stereographic projection of the data planes in the electron lens for sample No. 1. (b) Corresponding planes for sample No. 2. (c) Stereographic projections of contours of constant mass of the electron lens obtained from a ten-parameter interpolation expression. (d) Polar plot of masses predicted by the interpolation scheme for the (100) plane. Certain directions in real and reciprocal space are indicated in each figure.

with sample No. 1.

Only a few resonance peaks could be observed for mass curve L_τ^2 because this series was partially obscured by peaks corresponding to D_α^2; three or four resonance peaks were typically observed for W_τ^1. Both these mass curves are assigned to the τ orbits shown in Figs. 7(f) and 7(c). The cutoff points for these orbits toward the projection of the $(\bar{1}\bar{1}2)$ direction on the sample surface depend critically on the size of the T- and X-face openings and on the sample orientations, but could not be determined accurately for either sample because of the variety of other resonances observed in this region.

Mass curves $X_{\mu_2}^1$ and $K_{\mu_2}^2$ were characterized by only two or three resolved resonance peaks. These curves have been assigned to the bow-tie-shaped μ_2 orbits[12] which are approximately normal to the [001] and [010] directions in real space. These orbits pass around the bow-tie-shaped sections of the hole surface on either side of the X-face opening. Mass curve $J_{\mu_2}^2$ is tentatively assigned to a similar orbit centered near the projection of the [001] direction on the sample surface. The signals which give rise to these mass curves probably do not correspond to mass extrema. Apparently, the phases of the contributions to the surface impedance of the μ_2 orbits vary sufficiently slowly with k_H over the region for which these orbits are possible that the Fresnel-type integral representing the sum of these contributions yields an amplitude large enough to be observed. Bogle *et al.*[12] reported the observation of this orbit by magnetoacoustic attenuation experiments. Also, the masses G in Fig. 9 of Ref. 9 that were assigned tentatively to a μ orbit probably correspond to the μ_2 orbit. For their stated orientation, the μ_2 orbit about the (110) Brillouin-zone face is near its position of minimum mass while the suggested μ orbit cannot exist since it is cut off by the β arm along the [100] direction.

Two or three resonance peaks were typically observed for mass curve Z^1 but no orbit has been found to explain these signals.

When these experiments were carried out, the $\mu\gamma$, γ_2, and κ orbits had not previously been observed by any method. Recently Poulsen *et al.*[14] have observed the γ_2 and $\mu\gamma$ orbits in dHvA studies. These observations confirm the existence of these orbits and demonstrate that they are extremal orbits. The observation of several of these orbits passing through the X- and/or T-face openings implies that these openings must be approximately the size represented by the dotted lines in Fig. 7. Similar sizes are necessary to explain the results of Dishman and Rayne[11] and Poulsen *et al.*[14]

B. Crystal Orientation Using the α-Orbit Masses

The α-orbit data for the three lenses of Figs. 5 and 6 were superimposed, using symmetry, on one-quarter of one electron lens, as shown on the $\{100\}$ projections in Fig. 8. In Figs. 8(a) and 8(b), for samples No. 1 and No. 2, respectively, field directions in the sample surface are determined relative to the three distinct sets of electron lenses centered on the (100), (010), and (001) directions in reciprocal space and superimposed by symmetry on a single $\{100\}$ stereographic projection. The great circles representing the sample surface are reflected at the $\{1\bar{1}0\}$ mirror planes and, because the data have inversion symmetry, the ends of a great circle are equivalent points. Each of the great circles is labeled by the mass curve corresponding to it. The bar and arrow represent the positions of the projections of the $(\bar{1}\bar{1}2)$ direction on the sample surface and the sense of the magnetic field rotation, respectively.

The α-orbit data cross over six times for each sample in Figs. 8(a) and 8(b) and could therefore

be used to determine the orientations of these samples by adjusting the orientation for each such that the sum S of the squares of the mass differences at the crossover points were minimized. This was done by computer with a program in which the crossover points and mass differences at the crossovers were determined for an assumed orientation, and this orientation was then adjusted in successive iterations to minimize the error parameter S. The accuracy of this procedure was limited by the accuracy of the mass data; however, for both samples the coordinates θ, ϕ of $N(\theta,\phi)$ and a shift $\Delta\theta_s$ in θ_s were found to agree, within $\pm 1.0°$, with the corresponding values obtained from the open-orbit peak method discussed earlier. This good agreement demonstrates that the measured masses, at least at the crossover points, are internally consistent and confirms the crystal orientations.

C. Interpolation Scheme for the α-Orbit Masses

Because the α-orbit data sample wide ranges of the stereographic projections in Figs. 8(a) and 8(b), these data form a good basis for fitting a three-dimensional empirical interpolation scheme to the masses corresponding to the electron lens. The data were fitted simultaneously to the expression

$$[1/m^*(\alpha\beta\gamma)]^2 = A_1\alpha^2 + A_2\beta^2 + A_3\gamma^2 + A_4\alpha\gamma + A_5\alpha^2\beta^2 + A_5\alpha^2\gamma^2 + A_7\beta^2\gamma^2 + A_8\alpha\beta^2 + A_9\alpha^3 + A_{10}\alpha\gamma^3 , \quad (3)$$

where α, β, and γ are direction cosines relative to the orthogonal X, Y, and Z axes in Fig. 8(c). The axes Y and Z are parallel to the $(0\bar{1}0)$ and (100) directions, respectively. Equation (3) includes all terms to fourth order in the direction cosines which satisfy the mirror symmetry $m^*(Y) = m^*(\bar{Y})$ about the $(1\bar{1}0)$ plane in Fig. 8(c), and the inversion symmetry $m^*(\alpha\beta\gamma) = m^*(\bar{\alpha}\bar{\beta}\bar{\gamma})$ inherent in the mass data. The second-order terms in Eq. (3) are those in the Shockley expression for the effective mass of an ellipsoidal Fermi surface tipped an angle $0.5\arctan[A_4/(A_3 - A_1)]$ from the (100) direction toward the (111) direction. These terms themselves yield a fair approximation to the electron-lens masses. Coefficients and the rms deviation for the fourth-order ten-parameter fit are given in Table I, and the fit to the data is shown in Fig. 9. Contours of constant mass corresponding to this fit are given in the $\{100\}$ stereographic projection of Fig. 8(c), while a polar plot for masses in the (100) plane is given in Fig. 8(d). Masses predicted by the interpolation scheme for a variety of planes are shown in Fig. 10.

As illustrated in Figs. 8(c) and 10, the fourth-order fit shows that the position of the maximum mass is tipped 3.0° from the (001) direction toward the (111) direction in the $(1\bar{1}0)$ plane. The fit also

TABLE I. Coefficients for a fit of $(1/m^*)^2$ to Eq. (3), rms deviation in $m^* = 0.015 \sim 1.5\%$.

Coefficient	Value
A_1	2.289
A_2	2.652
A_3	0.320
A_4	9.635
A_5	−0.793
A_6	−0.019
A_7	−0.266
A_8	−9.405
A_9	−9.915
A_{10}	−9.835

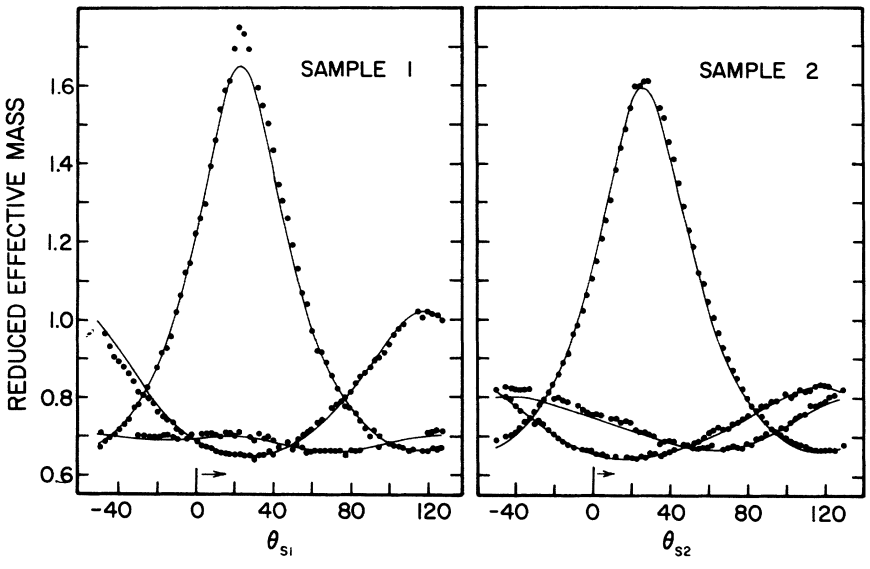

FIG. 9. Fourth-order fit to a α-orbit masses in samples No. 1 and No. 2.

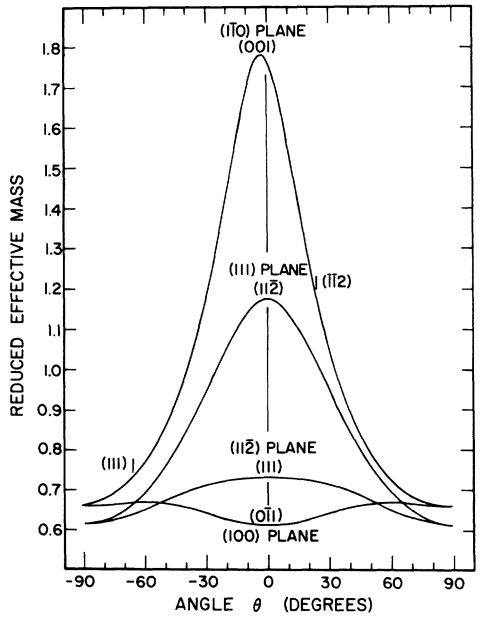

FIG. 10. α-orbit mass curves for several symmetry planes predicted by the interpolation scheme. Each curve is labeled by the plane to which it corresponds and by the crystallographic directions in reciprocal space at $\theta_s = 0°$.

shows that the broad mass minimum for $\vec{H}$ in the (1$\bar{1}$0) plane is also shifted 3.0° in the same sense. Maximum and minimum masses m^*/m_0 in this (1$\bar{1}$0) plane are 1.78 and 0.66, respectively, for the fourth-order fit.

The fourth-order fit also predicts, as shown in Figs. 8(d) and 10, that in the (100) plane the mass has a minimum value of 0.614 with $\vec{H}$ along the (0$\bar{1}$1) direction, and increases 9% to a value of 0.669 near [00$\bar{1}$] and [100]. This is clear evidence that the electron lens is not a surface of revolution about the line ΓL because mass values in the (100) plane are roughly proportional to the radius of the lens measured in the (100) plane and perpendicular to $\vec{H}$. Figure 8(d) shows that the electron lens has a minimum radius in the LU direction, and is pulled out approximately 9% in the LK direction. Brandt and Rayne[13] measured and Keeton and Loucks[15] predicted 6% and 10% increases, respectively, in the dHvA frequencies between the (0$\bar{1}$1) direction of reciprocal space and the [100] direction of real space. These results are in good agreement with the predictions of the fourth-order interpolation scheme presented here. This agreement, the small deviations between the fit and data in Fig. 9, and the wide ranges of the stereograms sampled by the measured planes in Figs. 8(a) and 8(b) show that the fourth-order interpolation scheme is reliable and useful for calculations of the α-orbit mass for any desired magnetic field direction. However, the systematic deviations of the fit from the data in Fig. 9 are slightly larger than expected from errors in the orientation or the mass measurements. These deviations indicate that better interpolation schemes might be obtained with a more complete set of data and the use of orthogonal basis functions composed of combinations of spherical harmonics chosen to satisfy the crystal symmetry.

D. Tipped-Field Cyclotron Resonance

A variety of field-tipping effects is illustrated for sample No. 2 in Figs. 11 and 12. The line shape for the fundamental of the D^2_α resonance changed significantly for $-0.035° < \alpha < +0.035°$. This indicates that sample No. 2 was flat to better than $\pm 0.035°$. The small-angle tipping effects are attributed to the Doppler-shifting mechanism discussed by Smith.[18]

The resonances D^2_α, F^2_α, and G^2_α all correspond to nearly ellipsoidal electron sections with low-mass spread, but exhibit very different sensitivity to tipping effects depending on the orientation of the lens with respect to both $\vec{H}$ and the sample surface. The lens corresponding to D^2_α was viewed

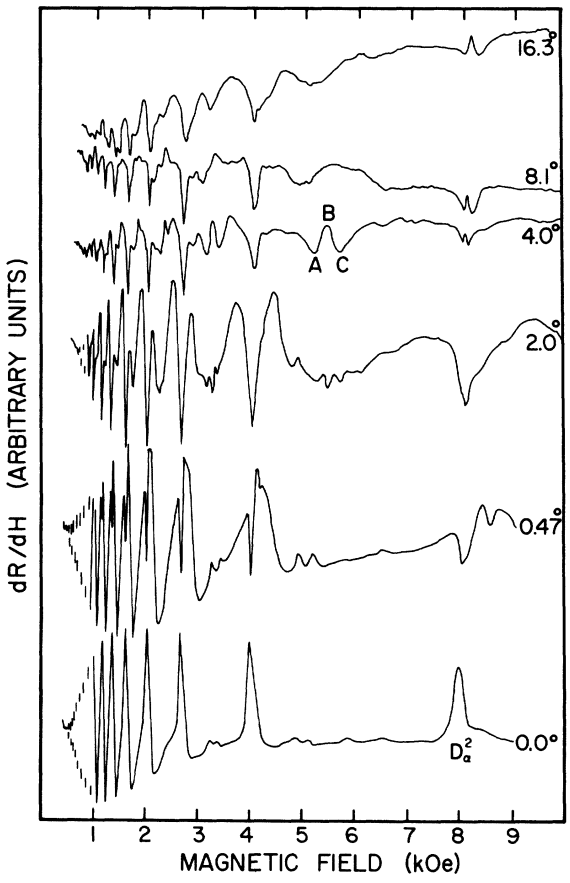

FIG. 11. Large field-tipping effects for $\theta_{s_2} = 120°$.

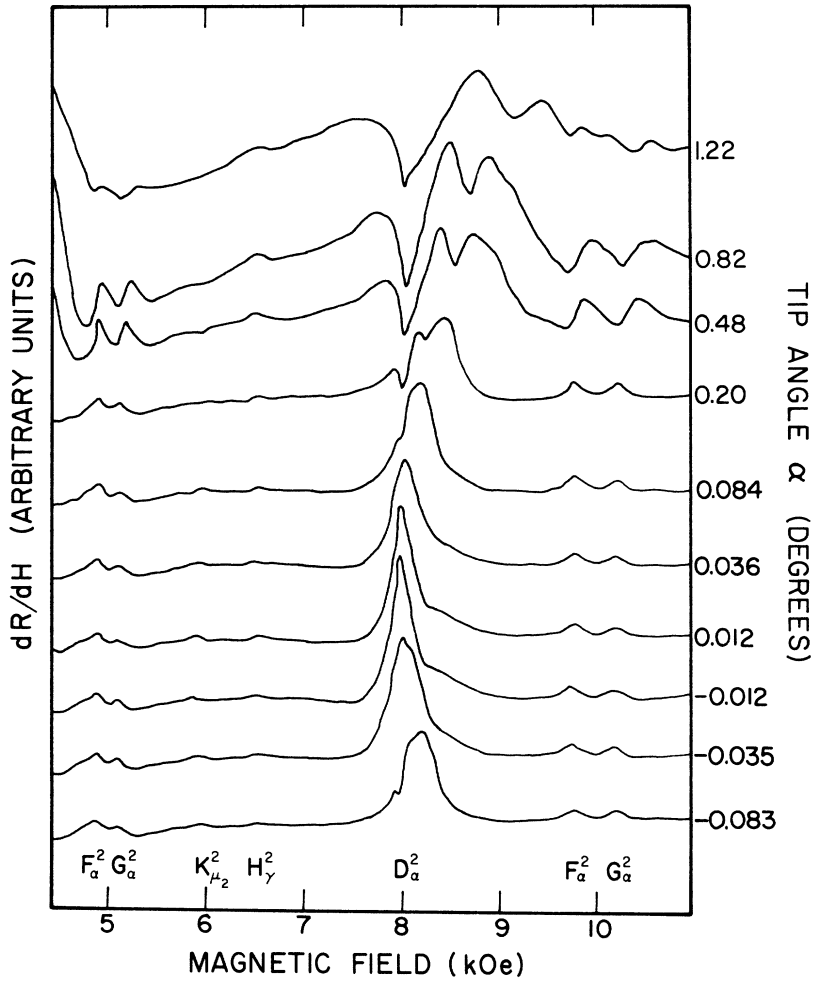

FIG. 12. Small-angle field-tipping effects for $\theta_{s_2} = 120°$.

almost edge on by $\vec{H}$ and a wide band of essentially stationary electrons contributed to the resonance with a very favorable geometrical factor so that strong, and eventually inverted, resonances were observed over a wide range of tip angles. The first peak on the high-field side of the split shifted 9.6%/deg for the fundamental but only 5.5%/deg for the second harmonic, while the position of the split remained virtually unchanged. Thus, where splitting of resonance peaks occurred from curved sample surfaces, Dixon and Datars[9] could have achieved greater accuracy by using the position of the split rather than the position of the dominant maximum to determine α-orbit masses. However, when this lens was viewed nearly along the (001) direction of reciprocal space so that only a very narrow band of stationary electrons contributed to the D_α^2 resonance the amplitudes observed with $\vec{j}_{rf} \perp \vec{H}$ decreased rapidly with increasing α as the nonstationary electrons drifted out of the skin depth. The F_α^2 and G_α^2 resonances corresponded to electron lenses which were tipped with respect to the sample surface. While these resonances showed slight signs of splitting, the major effects of field tipping were a shift in the position of the dominant peak to higher fields and resonance broadening.

As illustrated in Fig. 11, the D_α^2 resonance was inverted at large tip angles as expected for a Fermi-surface section, just as the electron lens, with low mass spread. The inversion of the resonant peak is explained by the increase of the effective depth of penetration of the electromagnetic field in the metal.[18,19] The masses corresponding to the inverted peaks were found to increase ~2% for $-10° < \alpha < +10°$, the change being consistent with changes in magnetic field direction as predicted from the ten-parameter interpolation scheme. In Fig. 3, positive tip angles are directed towards the $(1\bar{1}0)$ direction.

Over the same angular ranges, plots of $1/H_N$ vs $N(N = 1, 2, 3)$ for the features A-B-C in the $\alpha = 4°$ trace of Fig. 11 were essentially linear and had nearly the same slopes as similar plots for the inverted D_α^2 resonances. Therefore, these extra

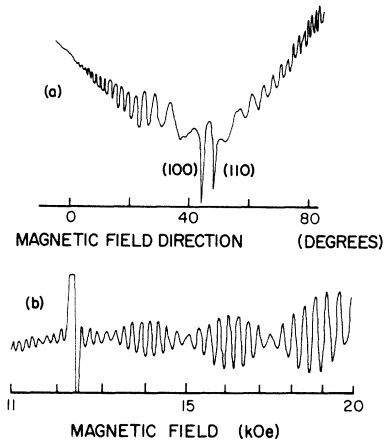

FIG. 13. Examples of dHvA-like quantum oscillations in dR/dH: (a) A field rotation trace including two induced-torque open-orbit peaks observed near the [010] direction from (100) and (110) open orbits. (b) A field scan trace illustrating beats between signals from two β arms, and a large signal at 12.4 kOe due to DPPH electron-spin resonance.

features A-B-C appear to have been associated with the electron lens responsible for mass curve D_α^2. For the indices $N = 1, 2, 3, \ldots$, the phase shifts ΔN for $1/H_N$-vs-N plots for A-B-C were grouped about $\Delta N = 0.5 \pm 0.1$. However, with $N = 3, 5, 7, \ldots$, $\Delta N = 0.0 \pm 0.1$ for A-B-C with a corresponding decrease in the slope of the $1/H_N$-vs-N plots by a factor of 2. The latter observations suggest the features A-B-C might have been due to mass-doubling current-sheet effects.[20] These effects are usually dominant with $\vec{j}_{rf} \parallel \vec{H}$ for limiting-point electrons. They arise from electrons near Fermi-surface limiting points which have the same cyclotron masses, essentially the same drift velocities v_D, and spiral along $\vec{H}$ on open helices of constant pitch but with varying radii. Such electrons are excited in the skin depth, then drift out of the skin depth, but are refocused each cyclotron period T_c at depths $d_n = nT_c v_D \sin\alpha$ (where n is an integer) into the sample. At these depths d_n they are again moving parallel to the sample surface and hence produce sheets of rf currents deep inside the sample. Electrons from the opposite side of the Fermi-surface drift through these current sheets toward the sample surface and, if $2\omega = m\omega_c$ where m is an integer, interact in phase with all of these current sheets. Similar effects can also be caused, at large angles of inclination, by resonant electrons which are not at limiting points if there is a velocity component along the field direction.[19] Then, in contrast to the case of the limiting point, resonance occurs for any polarization of the external field and the magnitude of the effect is smaller. Thus, it is possible that features A-B-C in Fig. 11 were caused by current sheets formed by electrons near extremal orbits of the electron lens.

The line shape of the D_α^2 fundamental in Fig. 11 differs in several respects from line shapes previously reported for large-angle tipping effects. First, there are two peaks rather than one peak on the high-field side of the split. Second, for the $\alpha = 2.0^\circ$ trace, there are slight oscillations apparent in the region of fields just above the split. Third, at larger tip angles, the inverted peak is itself apparently split into two parts. It may be that these features can be explained as arising from the specific shape and orientation of the electron lens in a theory such as that of Smith.[18] Alternatively, the oscillations might be associated with the propagation of plasmalike waves into the sample near AKCR.[21]

IV. QUANTUM OSCILLATION STUDIES

As previously reported,[9,22] oscillations like those shown in Fig. 13 were observed over wide ranges of sample orientation and of the tip angle between $\vec{H}$ and the sample surface. These oscillations were found to be periodic in reciprocal field and yielded dHvA frequencies F corresponding to the β-arm sections of the first-zone hole surface.

Here we summarize the frequencies measured for twenty off-symmetry planes in three crystals by the expression

$$\begin{aligned}(1/F)^2 = {} & 0.010\,\alpha^2 - 0.297\,\beta^2 + 1.828\,\gamma^2 \\ & + 3.224\,\alpha\gamma + 0.160\,\alpha^2\beta^2 - 0.136\,\alpha^2\gamma \\ & - 0.045\,\beta^2\gamma^2 - 3.169\,\alpha\beta^2\gamma \\ & - 3.295\,\alpha^3\gamma - 3.390\,\alpha\gamma^3. \qquad (4)\end{aligned}$$

In Eq. (4), α, β, and γ are direction cosines defining the field direction relative to the orthogonal axes X, Y, and Z in Fig. 14, respectively, and the coefficients were determined in a least-squares fit for which the three distinct sets of β-arm results were superimposed by symmetry on the stereographic projection normal to the [001] direction. The first three terms in Eq. (4) yield frequencies corresponding to a hyperboloidal Fermi-surface sheet oriented along Z, the fourth term allows for tip of the hyperboloidal sheet away from Z in the XZ (trigonal bisectrix) plane, while the remaining terms are the next-higher-order terms allowed by the crystal symmetry.

Agreement between this fit and the measured frequencies for a typical nonsymmetry plane is shown in Fig. 15 and is within experimental error for the determination of the orientation of that plane and of the frequencies. Equation (4) has been shown to yield frequencies which agree well with those measured in dHvA studies of the β-arm frequencies.[14]

The anisotropy of β-arm frequencies predicted from Eq. (4) are demonstrated by the 115-T fre-

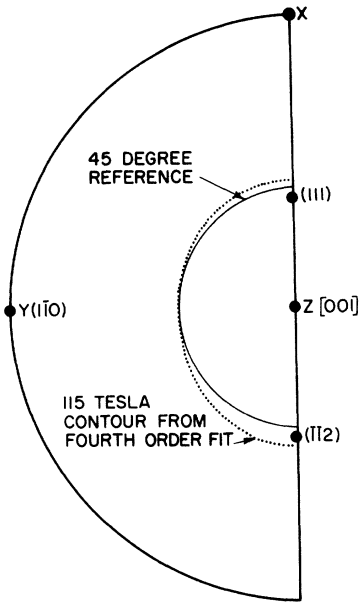

FIG. 14. The coordinates for, and a 115-T frequency contour calculated from, the fit to the β-arm dHvA frequencies represented in Eq. (4). Certain directions in real and reciprocal space are indicated.

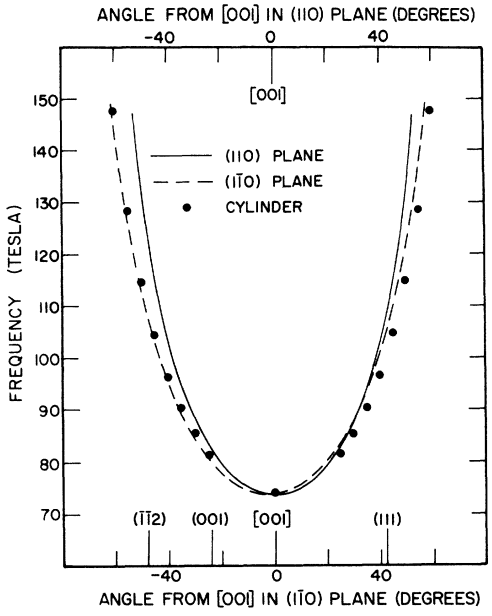

FIG. 16. dHvA β-arm frequencies predicted by Eq. (4) for the (110) and (1$\bar{1}$0) planes. The circles are frequencies corresponding to a cylindrical Fermi-surface sheet centered on [001] and having the same minimum frequency of 73.9 T. Certain directions in real and reciprocal space are indicated.

quency contour in Fig. 14, and the frequency spectra for the (110) and (1$\bar{1}$0) planes shown in Fig. 16. These figures show the β arm flares out most rapidly in the (110) section where it joins the rest of the hole surface. This is expected, since this section includes the shape of the X-face opening in the hole surface.

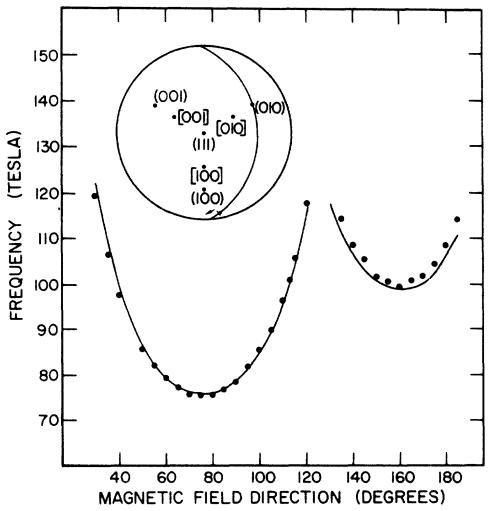

FIG. 15. dHvA β-arm frequencies for a sample oriented as shown in the stereogram. The solid line is the fit given by Eq. (4). The sense of magnetic field direction is indicated by the arrow in the stereogram.

Previously, oscillations such as those studied here have been attributed to "quantum oscillations" in the microwave surface impedance in mercury[9] and aluminum.[20] Such oscillations are expected to occur for electrons on cyclotron orbits which are very nearly stationary and for which the real-space radii are less than the skin depth.[23] The β arms of mercury satisfy these conditions well; not only is the radius of the real-space orbit sufficiently small ($\sim 1 \times 10^{-5}$ cm at 20 kOe), but also the β arms are very nearly cylindrical so that a wide band of electrons having nearly stationary orbits contribute in phase. In the present experiment, however, we conclude that the oscillations observed arise, in part, from the effect of torque on the sample arising from the dHvA effect corresponding to the β arms. Such torque on the sample can affect the cavity Q and thus generate the observed signal by slightly changing the sample position. Evidence for the existence of such torque effects include the observations: (i) that the amplitudes increased considerably when the sample was mounted less tightly in the cavity, and vice versa, (ii) that, even for a tightly mounted sample, the amplitudes were very sensitive to tapping the helium Dewar lightly and often were not reproducible, and (iii) that, for one sample, the amplitudes changed little after the sample surface was very severely scored with a cotton swab, thus indicating a bulk effect such as torque.

The oscillations persisted when $\vec{H}$ was parallel to $\langle 001 \rangle$ directions where the frequency F is an absolute minimum and the torque effects must disappear. Thus the oscillations appear to have been, at least in part, due to quantum oscillations of the microwave surface impedance. Because of the complications arising from the torque effects, the dependence of these quantum oscillations on the microwave polarization, or on the tip angle between $\vec{H}$ and the sample surface, could not be studied in detail.

V. CONCLUSIONS

AKCR studies have been carried out with two very flat mercury single crystals. Possible errors in the effective masses arising from field-tipping effects were small because the magnetic field was aligned accurately parallel to flat sample surfaces. Several new orbits ($\mu\gamma$, γ_2, κ, μ_2, and ϵ_1) were observed for the first time by AKCR. Measurements in nonsymmetry planes permitted the development of a three-dimensional interpolation scheme for the α-orbit masses. This interpolation scheme showed that the second-zone electron lens is tipped 3° out of the (100) plane toward the [111] direction, and that there is a 9% anisotropy of the mass in the (100) plane.

Cyclotron effective masses of ten orbits were measured in two off-symmetry crystallographic planes. The minimum measured masses of the orbits are summarized in Table II. These masses are not the absolute minima for the orbits, but some are close to these minima. The reduced masses m^*/m_0 ranged from 0.62 to 2.2. These masses will be useful for estimating the anisotropy of the electron-phonon mass enhancement factor $1+\lambda$. Here, we note only that estimates based on the minimum α-orbit mass of 0.615 for $\vec{H} \parallel (1\bar{1}0)$ yield $1+\lambda$ values of 2.3 and 2.2 relative to the RAPW model of Keeton and Loucks[15] and to the model of Bogle *et al.*[12] These values of $1+\lambda$ are lower than the McMillan and Rowell value[24] of $1+\lambda \sim 2.6$ indicating possible discrepancies in the two determinations of $1+\lambda$ or anisotropy of the electron-phonon mass enhancement.

Open-orbit induced-torque effects were shown to generate apparent peaks in dR/dH which could be used to determine accurately the crystal orientation within the experimental apparatus. Similarly, dHvA torques were found to contribute to signals arising from quantum oscillations of the microwave surface resistance. Studies of these oscillations yielded a three-dimensional empirical interpolation scheme for the β-arm dHvA frequencies.

Studies of the effect of tipping the applied magnetic field out of the sample surface indicate that there was anomalous penetration of the electromagnetic field into the metal.

TABLE II. Minimum cyclotron effective masses of orbits measured in two off-symmetry crystallographic planes.

Orbit	Field direction	AKCR reduced mass
α	$(1\bar{1}0)$[a]	0.614[b]
	[110]	0.661[b]
	(110)	0.700[b]
	[111]	0.733[b]
	(001)	1.77[b]
γ	18° from $(11\bar{2})$ toward (110)[a]	$\lesssim$ 0.65[c]
τ	$(\bar{1}01)$[a]	< 0.71[d]
μ	$(\bar{1}\bar{1}2)$	1.24
μ_2	[001][a]	0.99[e]
ϵ_1	(001)[a]	2.23[f]
γ	22° from $(11\bar{2})$ toward (110)	1.47[g]
$\mu\gamma$	(−85.0, −37.8)[h]	1.42
κ	(90.0, 38.5)[h]	1.1

[a]Directions of minimum AKCR mass for the orbit.
[b]From the 10-parameter α-mass interpolation scheme for the lens normal to the (001) direction.
[c]Misoriented 6° from $(1\bar{1}0)$ plane; from Fig. 5.
[d]Misoriented 21.5° from $(\bar{1}01)$ toward $(\bar{1}\bar{1}2)$; from Fig. 6.
[e]Misoriented 14.8° from $(1\bar{1}0)$ plane; from Fig. 5.
[f]Misoriented 8.2° from $(1\bar{1}0)$ plane; from Fig. 5.
[g]Misoriented 7.5° from $(1\bar{1}0)$ plane; from Fig. 5.
[h]Coordinates (θ, ϕ) refer to Fig. 3.

ACKNOWLEDGMENTS

We wish to thank Dr. A. E. Dixon for fruitful discussions. Research support from the National Research Council of Canada (NRC) and fellowships from the NRC (to W. R. D. and R. G. P.) and the International Nickel Company of Canada (to R. G. P.) are gratefully acknowledged.

†Research Supported by the National Research Council of Canada.

*International Nickel Company of Canada Predoctoral Fellow. Present address: University of Sussex, Brighton, England.

[1]N. W. Ashcroft and J. W. Wilkins, Phys. Letters 14, 285 (1965).
[2]M. J. G. Lee, Phys. Rev. B 2, 250 (1970).
[3]T. M. Rice, Ann. Phys. (N.Y.) 31, 100 (1965).
[4]M. Yu. Azbel' and E. A. Kaner, J. Phys. Chem. Solids 6, 113 (1958).
[5]R. G. Chambers, Proc. Phys. Soc. (London) 86, 305 (1965).
[6]A. F. Kip, D. N. Langenberg, and T. W. Moore, Phys. Rev. 124, 359 (1961).
[7]R. G. Poulsen and W. R. Datars, Solid State Commun. 8, (1970); in *Proceedings of the Twelfth International Conference on Low Temperature Physics, Kyoto*, 1970, edited by Eizo Kauda (Academic Press of Japan, Kyoto, 1971), p. 6-617.

[8]J. F. Koch, R. A. Stradling, and A. F. Kip, Phys. Rev. 133, A240 (1964).
[9]A. E. Dixon and W. R. Datars, Phys. Rev. 175, 928 (1968).
[10]W. R. Datars and A. E. Dixon, Phys. Rev. 154, 476 (1967).
[11]J. M. Dishman and J. A. Rayne, Phys. Rev. 175, 928 (1968).
[12]T. E. Bogle, J. B. Coon, and C. Grenier, Phys. Rev. 177, 1122 (1969).
[13]G. B. Brandt and J. A. Rayne, Phys. Rev. 148, 644 (1966).
[14]R. G. Poulsen, J. S. Moss, and W. R. Datars, Phys. Rev. B 3, 3107 (1971).
[15]S. C. Keeton and T. L. Loucks, Phys. Rev. 152, 548 (1966).
[16]J. Jones and W. R. Datars (unpublished).
[17]J. S. Moss and W. R. Datars, Phys. Letters 24A, 630 (1967).
[18]D. A. Smith, Proc. Roy. Soc. (London) A297, 205 (1967).
[19]E. A. Kaner and A. Ya Blank, J. Phys. Chem. Solids 28, 1735 (1967).
[20]F. W. Spong and A. F. Kip, Phys. Rev. 137, 431 (1965).
[21]W. M. Walsh, in *Electrons in Metals*, Vol. 1 of *Solid State Physics*, edited by J. F. Cochran and R. R. Haering (Gordon and Breach, New York, 1968), p. 144.
[22]R. G. Poulsen, A. E. Dixon, and W. R. Datars, Bull. Am. Phys. Soc. 12, 703 (1967).
[23]M. Ya. Azbel', J. Phys. Chem. Solids 7, 105 (1958).
[24]W. L. McMillan and J. M. Rowell, in *Superconductivity*, edited by R. D. Parks (Marcel Dekker, New York, 1967).

PHYSICAL REVIEW B VOLUME 4, NUMBER 12 15 DECEMBER 1971

Electrical Resistivity of Potassium from 1 to 25 °K†

J. W. Ekin* and B. W. Maxfield‡
Laboratory of Atomic and Solid State Physics, Cornell University, Ithaca, New York 14850
(Received 19 July 1971)

Low-temperature electrical-resisitivity data are presented for pure and impure potassium samples [$8000 \gtrsim \rho(20\ °C)/\rho(0\ °K) \gtrsim 100$] and compared with theory. The experimental and theoretical results are tabulated, interpreted, and compared with the work of others. In particular, the resistivity data of the impure samples exhibited only relatively minor deviations from Matthiessen's rule and did not differ appreciably in temperature dependence from the resistivity data of the pure samples. Experimental details are presented and a short study of quenching effects has been made.

I. INTRODUCTION

The temperature and impurity dependence of the electrical resistivity of a metal can act, in many cases, as a definitive test for establishing the state of our present theoretical understanding of low-temperature transport mechanisms. In particular, questions concerning electron-phonon umklapp scattering processes and electron-impurity scattering processes have prompted this study of the low-temperature electrical resistivity of potassium. Previous treatments of these scattering mechanisms have been mostly qualitative and many discrepancies between theoretical prediction and experimental observation have emerged.

Recently, we reported the first detailed agreement between theory and experiment as concerns our understanding of the role of umklapp processes in determining the low-temperature electrical resistivity of potassium in particular and more generally of the ideal monovalent metals.[1] This paper presents additional resistivity data on less-pure samples, an explicit tabulation of the earlier reported results, and a more extensive discussion of other aspects of these results.

The details of sample preparation, cryostat design, and instrumentation are discussed in Sec. II. In Sec. III the experimental results are presented: The results of a short study of quenching effects are reported in Sec. III A; the experimental results of the purer potassium samples are tabulated and compared with the work of others in Secs. III B and III C; and in Sec. III D results from measurements on less-pure samples and alloys are discussed along with some of their more general implications as regards deviations from Matthiessen's rule. Last, in Sec. IV the theoretical results are summarized, tabulated, and several interpretive remarks are presented.

II. EXPERIMENTAL RESULTS

A. Sample Preparation

Prior to extrusion of the polycrystalline wire samples, an etching solution of 2% secondary butyl alcohol in xylene was used to remove surface contamination from the bulk material. Extrusion was done at room temperature under dehydrated paraffin oil. Wire diameters were maintained at approximately ten times the maximum low-temperature electron mean free path and in no case were sig-